Synsint Research Group

Available online at www.synsint.com

Synthesis and Sintering

ISSN 2564-0186 (Print), **ISSN** 2564-0194 (Online)

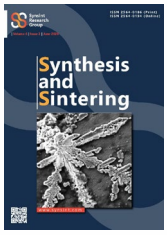

Research article

Numerical investigation of die thickness and height effects on temperature distribution and energy consumption during spark plasma sintering of TiB_2

Ramin Meshkabadi [a,*], **Milad Sakkaki** [b], **Vahid Pouyafar** [b]

[a] *Faculty of Advanced Technologies, University of Mohaghegh Ardabili, Ardabil, Iran*
[b] *Faculty of Mechanical Engineering, University of Tabriz, Tabriz, Iran*

A B S T R A C T

Precise temperature control during spark plasma sintering is critically important because it directly affects densification kinetics, microstructural evolution, and the final mechanical properties of the sintered component. However, direct temperature measurement inside the tooling remains experimentally inaccessible, and the complex interactions among electro-thermal coupling, contact resistances, and tooling geometry make process optimization particularly challenging. Numerical and experimental studies specifically addressing conductive TiB_2 ceramics remain limited. This work establishes a coupled electro‑thermal finite element model, validated against experimental pyrometer data, to evaluate the effects of die wall thickness (7 mm, 14 mm, and 28 mm) and die height (11 mm, 22 mm, and 35 mm) on current and temperature distribution, thermal uniformity, heating rates, and energy consumption while fully incorporating electrical and thermal contact resistances and graphite sheet interlayers. Results demonstrate that die height dominates thermal performance. Increasing height from 11 mm to 35 mm reduces the sample center temperature from 1932 °C to 1754 °C, while increasing the die surface radiative loss from 1675 W to 3592 W. The heating rate at the sample center decreases from 140 °C/min to 116 °C/min as height increases to 35 mm, while the die surface heating rate drops more sharply from 130 °C/min to 80 °C/min, widening the difference from 10 °C/min to 36 °C/min. In contrast, increasing wall thickness from 7 mm to 28 mm raises radiative loss more modestly from 2351 W to 2792 W, while the sample center temperature declines from 1992 °C to 1878 °C. The heating rate at the sample center decreases from 150 °C/min to 116 °C/min, and the die surface heating rate drops from 120 °C/min to 76 °C/min. The required input power to maintain 1900 °C at the sample center is lowest for the 7 mm thick die (9596 W). For die height, the 22 mm configuration minimizes power consumption (10103 W) by surrounding the punch and reducing heat accumulation inside it, whereas increasing the height to 35 mm yields no additional energy savings due to increased die surface losses. These findings quantitatively establish die height as the primary lever for controlling current focusing and thermal efficiency.

KEYWORDS

Spark plasma sintering
Titanium diboride
Finite element method
Contact resistance
Temperature distribution
Energy efficiency

OPEN ACCESS

* Corresponding author. *E-mail address:* R_meshkabadi@uma.ac.ir (R. Meshkabadi)
Received 27 March 2026; Received in revised form 22 June 2026; Accepted 26 June 2026.

https://doi.org/10.53063/synsint.2026.62336

Nomenclature

Symbol	Description	Symbol	Description
UHTC	Ultra-high temperature ceramic	c_p	Specific heat capacity (J/kg.K)
SPS	Spark plasma sintering	r	Radial coordinate (mm)
TiB_2	Titanium diboride	z	Axial coordinate (mm)
TCR	Thermal contact resistance (m².K/W)	q_i	Heat generation rate per unit volume (Joule heating) (W/m^3)
ECR	Electrical contact resistance (Ω.m²)	i_r	Current density in radial direction (A/m^2)
J	Current density (A/m^2)	i_z	Current density in axial direction (A/m^2)
E	Electric field (V/m)	q_c	Convective heat flux (W/m^2)
R	Electric resistance (Ω)	h_c	Convective heat transfer coefficient ($W/m^2.K$)
i	Current (A)	T_s	Convection heat transfer surface temperature (K)
U	Electric potential, voltage (V)	T_w	Water temperature (K)
σ	Electrical conductivity (S/m)	σ_s	Stefan-Boltzmann constant ($5.67.10^{-8}$ W/m^2K^4)
T	Temperature (°C)	ε	Emissivity
K	Thermal conductivity (W/m.K)	T_e	Radiative heat transfer surface temperature (K)
K_r	Thermal conductivity in radial direction (W/m.K)	T_a	Ambient temperature (K)
K_z	Thermal conductivity in axial direction (W/m.K)	$\dot{q}_c$	Heat flux due to TCR (W/m^2)
ρ	Density (kg/m^3)	J_c	Electric current density passing through the contact surface (A/m²)
t	Thickness (mm)	τ	Time
h	Height (mm)	DC	Direct current

1. Introduction

As technology advances, the performance required from materials increasingly surpasses the capabilities of conventional ones. This need has prompted the development of advanced ceramics. Ultra‑high temperature ceramics (UHTCs) feature melting points exceeding 3000 °C, thermal shock resistance, stability at high temperatures, excellent mechanical strength, corrosion resistance, and notable thermal and electrical conductivities [1, 2]. Due to their ceramic nature and extremely high melting points, UHTCs cannot be produced by conventional methods such as casting; instead, powder‑based processing is the main manufacturing route [3]. The typical production sequence consists of four steps: powder preparation, mixing and homogenization of additives, compaction into a desired shape, and finally heating and sintering [4]. Among the common sintering techniques are pressureless sintering, microwave sintering, hot pressing, hot isostatic pressing, and spark plasma sintering (SPS) [5]. Although these methods share the same basic stages, they differ in how heat and pressure are applied.

SPS, also referred to as field‑assisted sintering, is a common technique for producing UHTCs. In this process, densification is achieved through the simultaneous application of axial pressure and an electric current. The primary source of heat is Joule heating as current passes through resistive parts [6]. In contrast to hot pressing, which relies on external heating elements, SPS generates heat internally via current flow through the tooling and, when the powder is electrically conductive, through the powder itself [7]. This internal heat generation leads to distinctive microstructural features and provides benefits including short processing times, high heating rates, preservation of the original powder morphology, reduced grain growth, high relative density, and enhanced mechanical properties [8, 9]. Once current is applied, the heating path is determined by the electrical conductivity of the sample. For non‑conductive powders, heat is produced in the tooling and then conducted to the specimen. For conductive powders, current also passes through the sample, producing direct internal Joule heating [10]. A water‑cooling system is used to avoid overheating of the equipment. Important process parameters include current and current density, temperature, heating and cooling rates, electrical and thermal contact resistances, applied pressure, material characteristics, and time. SPS is generally carried out in a vacuum environment to prevent undesired chemical reactions [7].

The effectiveness of SPS is critically dependent on precise temperature control, as it directly governs the densification kinetics, dictates the microstructural evolution, and ultimately determines the final mechanical properties and overall performance of the sintered component [11]. Moreover, direct temperature measurement during SPS remains challenging and is often restricted to a few locations. Consequently, experimental optimization can be expensive and time‑consuming. Numerical simulation offers an efficient way to explore temperature and current distributions within the tooling and the specimen throughout the sintering process. It can determine the current needed to achieve a given sintering temperature for different sample shapes, thereby aiding energy optimization and process development. Lee et al. [12], in an experimental-numerical study on conductive zirconium nitride (ZrN) powder, investigated the effect of electric current on the densification mechanism during SPS. By embedding a thermocouple directly into the powder, they measured the actual sample temperature during SPS and showed that the powder temperature during the cycle was up to 141 °C higher than the temperature measured at the graphite die. Using finite element modeling and calculating the effective current density based on interparticle neck area evolution, they developed a new constitutive equation for SPS that explicitly incorporates the electric current term. They reported SPS significantly accelerates the densification rate, such that full density was achieved in SPS at 1500 °C while hot pressing

required 1900 °C. Earlier studies have demonstrated that contact resistances significantly affect temperature predictions. Omitting electrical and thermal contact resistances (ECR and TCR) in simulations can lead to significant temperature underestimations [13]. Manière et al. [14], in a finite-element modeling of electro-thermal contacts in the spark plasma sintering (SPS) process, demonstrated that ECR increases the overall system temperature by approximately 100 °C, while TCR on both sides of the graphite Papyex sheet traps heat within it and generates intense localized heating. Fattahi et al. [15] performed a numerical study on the SPS of TiB_2 using a finite element approach. They reported a radial temperature difference of approximately 70–75 °C between the sample center and the die surface at a sintering temperature of around 2000 °C. In their model, TCR was implemented only at the punch/spacer interface, represented as an equivalent layer with a thickness of 0.1 mm and a thermal conductivity of 0.04 W/m.K. ECR was assumed to be zero at the punch/die interface, and no separate graphite sheet layer was included. Their simulation was based on previously established frameworks and was not experimentally validated specifically for TiB_2. However, most existing numerical studies have either focused on contact resistances in isolation or examined die geometry without fully coupling both effects. Moreover, investigations of how die thickness influences thermal uniformity and energy consumption for titanium diboride (TiB_2) UHTCs remain scarce. The present work develops a coupled electro‑thermal simulation of SPS for (TiB_2), and the primary objective is to investigate how variations in die geometry affect current distribution, temperature field, and energy consumption during the SPS of TiB_2 ceramics, while fully accounting for ECR, TCR, and the presence of the graphite sheet. TiB_2 is a conductive UHTC characterized by a melting point of 3225 °C, low density, high hardness, high Young's modulus, and satisfactory thermal and electrical conductivities [16, 17]. These characteristics make TiB_2 suitable for aerospace, thermal protection systems, cutting tools, wear‑resistant parts, armor, and electrode applications [17–20]. A particular focus is placed on the effect of die thickness and height on thermal uniformity and power demand. This study not only fills a gap in the literature regarding the combined influence of contact resistance and die geometry but also provides practical guidelines for selecting die dimensions to achieve homogeneous sintering with optimum energy consumption.

2. Materials and methods

2.1. Experimental procedure

A commercial TiB_2 powder with a particle size ≤5 µm and a purity of >99% was used as the starting material. Sintering was performed in an SPS device (SPS-20T-10, China) using a graphite die, punch, spacer, and copper electrodes. A 1 mm thick graphite sheet was placed between the powder and the tooling surfaces to prevent contamination and facilitate ejection. The powder was consolidated under vacuum at a uniaxial pressure of 40 MPa, with the punch temperature set to 1900 °C and a dwell time of 7 minutes at the peak temperature. For validation purposes, temperatures were recorded at point A (see Fig. 1) using optical pyrometers. Reliable readings were obtained only for temperatures exceeding 1000 °C. After cooling to room temperature, the final sintered compact measured 30 mm in diameter and 7 mm in thickness.

2.2. Numerical simulation

2.2.1. Geometry and material properties

The computational domain includes all relevant components of the SPS tooling assembly, namely the upper and lower copper electrodes, graphite spacers, graphite punches, the graphite die, and the TiB_2 sample. Owing to the axisymmetric nature of the geometry and the applied boundary conditions, a 2D axisymmetric representation was adopted, as shown in Fig. 1. The reference geometry (used for model validation) corresponds to a die wall thickness of 14 mm and a die height of 22 mm. For parametric studies, die wall thicknesses of 7, 14, and 28 mm and die heights of 11, 22, and 35 mm were independently examined. Three characteristic points are indicated in Fig. 1: Point A on the outer surface of the upper punch (the pyrometer monitoring location), point B on the outer lateral surface of the die at the mid‑height of the sample, and point C at the center of the TiB_2 sample. All dimensional values are directly readable from the scale bar provided in Fig. 1. Given the wide temperature range from the cooled electrodes to the hot sample, using constant material properties would introduce significant errors in the simulation. Therefore, temperature‑dependent electrical and thermal properties were adopted for components, as summarized in Table 1.

2.2.2. Governing equations

In spark plasma sintering, Joule heating is generated by the flow of electric current through the material. Consequently, precise knowledge of the local current density is necessary. The temperature distribution is determined by solving a set of two coupled governing equations: one for charge conservation and one for energy conservation. Eq. 1 describes the steady‑state behavior of direct-current flow (Maxwell's equation) under the assumption of a purely resistive medium.

Table 1. Temperature-dependent properties of graphite, copper, and TiB_2 (temperature in Kelvin).

Material	Density (kg/m^3)	Heat capacity (J/kg.K)	Thermal conductivity (W/m.K)	Electric resistivity (Ω.m)
TiB_2 [15]	4520	$976 + 0.21\times(T-273) - 426\times10^{-0.008\times(T-273)}$	$77.3 + \frac{(8270\times10^{-0.002\times(T-273)})}{410+(T-273)}$	$\frac{(10.05+0.0431\times T)}{10^8}$
Graphite [14]	$1904 - 0.01414\times T$	$34.27 + 2.72\times T - 9.6\times10^{-4}\times T^2$	$123 - 6.99\times10^{-2}T + 1.55\times10^{-5}T^2$	$1.7\times10^{-5} - 1.87\times10^{-8}T + 1.26\times10^{-11}T^2 - 2.44\times10^{-15}T^3$
Copper [21]	8960	$355.3 + 0.1\times T$	420.66+0.07× T	$\frac{(5.5+0.038\times T)}{10^9}$

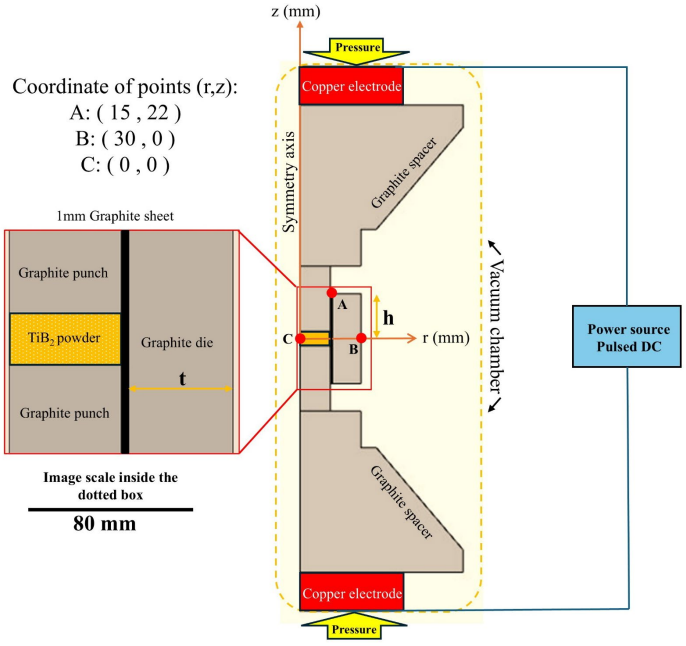

Fig. 1. Schematic of the axisymmetric computational domain showing the geometry and dimensions.

$$\nabla J = \nabla(\sigma E) = \nabla(-\sigma \nabla U) = 0 \quad (1)$$

Expressed in cylindrical coordinates, the governing equation for electric current is written as Eq. 2:

$$\frac{1}{r}\frac{\partial(r i_r)}{\partial r} + \frac{\partial i_z}{\partial z} = 0 \quad (2)$$

Given the cylindrical geometry, an axisymmetric energy balance is appropriate. The conservation of energy, including Joule heating, in cylindrical coordinates is written as Eq. 3:

$$\rho C_p \frac{\partial T}{\partial \tau} = \frac{1}{r}\frac{\partial}{\partial r}\left(r k_r \frac{\partial T}{\partial r}\right) + \frac{\partial}{\partial z}\left(k_z \frac{\partial T}{\partial z}\right) + q_i \quad (3)$$

In Eq. 3, the term q_i denotes the volumetric heat source due to Joule heating, which is expressed as:

$$q_i = J.E = \sigma(\nabla U)^2 \quad (4)$$

The compact form of the coupled thermos-electrical governing equations is expressed by Eq. 5.

$$\nabla.(-k\nabla T) + \rho C_p\left(\frac{\partial T}{\partial \tau}\right) = \sigma(\nabla U)^2, \ \nabla.(\sigma.\nabla U) = 0 \quad (5)$$

2.2.3. Boundary conditions and initial values

The initial temperature of the entire SPS assembly is set to 300 K, and the electric potential is initially zero on both electrodes and throughout the device. To solve the coupled governing equations, appropriate electrical and thermal boundary conditions are applied as illustrated in Fig. 2. Convective cooling provided by the water circulation system is imposed on the upper and lower electrodes, and this is described by the convective heat flux boundary condition given in Eq. 6.

$$q_c = h_c(T_s - T_w) \quad (6)$$

A convective heat transfer coefficient of 880 $W.m^{-2}.K^{-1}$ is imposed on the upper and lower surfaces of the electrodes [22]. Since the entire setup is placed inside a vacuum chamber, any convective heat loss from the lateral surfaces is ignored; only radiative heat transfer is taken into account at those boundaries. Owing to horizontal symmetry, the radiative flux emitted from one horizontal side is absorbed by the opposite side, and therefore these surfaces are considered thermally insulated. The radiative exchange is described by the Stefan-Boltzmann law as expressed in Eq. 7.

$$q_r = \sigma_s.\varepsilon.(T_e^4 - T_a^4) \quad (7)$$

The emissivity of graphite is set to 0.8. Pure polished copper has an emissivity of approximately 0.03; however, the copper electrode employed in this work was heavily oxidized, giving it a dark appearance that significantly raises its surface emissivity. For such oxidized copper surfaces, reported emissivity values typically lie between 0.6 and 0.8. Accordingly, an average value of 0.7 was adopted for the copper electrode in the present simulations. The thermal contact conditions at the internal interfaces are expressed by Eq. 8.

$$\dot{q}_c = \frac{1}{TCR}(T_1 - T_2) \quad (8)$$

The external surfaces of the device are treated as electrically insulated. Current is imposed on the upper electrode, while the lower electrode is set to ground (V = 0). Electrical contact resistance values for both vertical and horizontal interfaces were adopted from the experimental measurements reported by Wei et al. [23] and assigned to the respective internal contacts. The electrical contact condition at these interfaces is imposed using Eq. 9:

$$J_c = \frac{1}{ECR}(U_1 - U_2) \quad (9)$$

2.2.4. TCR and ECR calibration

A systematic procedure was followed to identify appropriate ECR and TCR values. Initial simulations were performed neglecting all contact resistances, which resulted in temperatures significantly below the

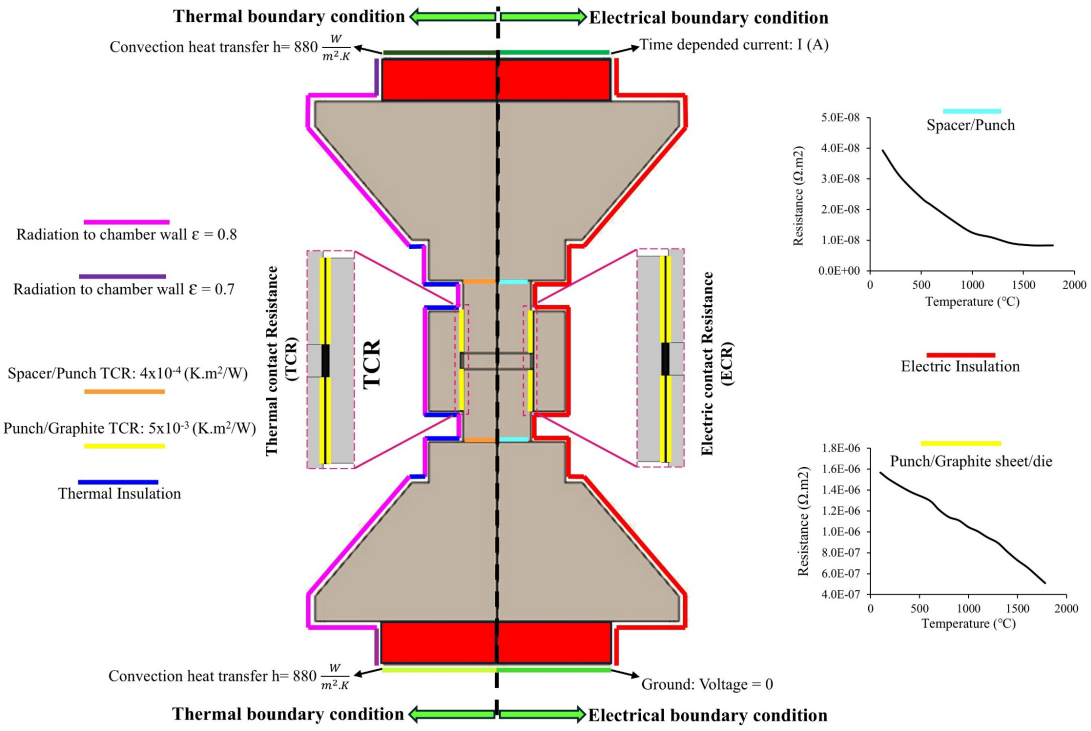

Fig. 2. Thermal (left) and electrical (right) boundary conditions applied to the SPS model.

experimental readings. Subsequently, ECR and TCR were added separately at each interface, and their influence on the temperature distribution was evaluated by comparing the simulated results with experimental data. Candidate values for the contact resistances were extracted from earlier experimental investigations performed under similar processing conditions. The calibration process was considered complete once the closest possible agreement between simulation and experiment was attained.

At the punch/sample interface, the applied axial pressure (40 MPa) combined with the high sintering temperature (1900 °C) ensures intimate physical contact, making both ECR and TCR negligible. This is consistent with previous studies reporting that at temperatures above 800 °C and pressures around 50 MPa, contact resistances approach near-zero values and can be safely ignored [14, 24]. At the copper electrode/spacer interface, several factors justify neglecting contact resistances. Copper's low microhardness promotes plastic deformation under pressure, enhancing contact, while its high electrical and thermal conductivity further minimizes resistance. Additionally, the large electrode diameter results in low current density at this interface, diminishing the significance of ECR. At the sample/graphite foil/die interface, although the graphite sheet is present, the uniaxial pressure (40 MPa) transmits approximately 40–60% of the axial load to the radial direction, generating significant lateral pressure. This, together with the high temperature (up to 1900 °C), substantially reduces contact resistance [24, 25]. Furthermore, due to the high electrical conductivity of the TiB_2 sample, the electric current preferentially follows the low-resistance path through the sample thickness (between the upper and lower punches) rather than deviating laterally through the sample/graphite sheet/die interfaces.

2.2.5. Solution methodology

As shown in Fig. 3, the computational domain was discretized using triangular elements. To accurately capture the effects of electrical and thermal contact resistances, the mesh was locally refined at the critical interfaces, namely the punch/die, sample/sheet/die, punch/spacer, and spacer/electrode boundaries. A mesh‑independence study was then performed to ensure that the numerical results are not artifacts of the discretization and do not depend on the element count. As presented in Table 2, increasing the number of elements beyond 10210 produced negligible changes in the predicted temperatures; therefore, this mesh size was selected for all subsequent simulations, providing a reliable balance between accuracy and computational cost.

3. Results and discussion

To verify the reliability of the numerical model, the simulated temperature at point A (the pyrometer monitoring point on the punch) was compared with the experimental measurements obtained during the SPS process. The comparison is presented in Table 3. The simulated temperatures show good agreement with experimental data. A deviation of about 100 °C at low temperatures (below 1000 °C) is attributed to the pyrometer inaccuracy. Above 1000 °C, the difference decreases significantly, reaching less than 30 °C on average and converging to within 4 °C during the dwelling stage. This confirms that the calibrated numerical model reliably captures the thermal behavior of the TiB_2 SPS process.

Table 2. Mesh independence results at points A and C (Fig. 1) for various mesh sizes.

Mesh number	828	1772	4108	10210	15558
T_A	1988	1988	1901	1901	1900
T_C	1930	1932	1953	1936	1935

Table 3. Comparison of experimental and simulated temperatures at point A (pyrometer monitoring point on the punch) during the SPS cycle.

Time (s)	536	725	841	945	1120	1266
T_A (Exp)	1038	1480	1825	1918	1900	1900
T_A (Sim)	938	1526	1827	1892	1904	1900

3.1. Effect of die thickness and height on current and temperature distribution

3.1.1. Effect of die thickness (t)

Fig. 4 presents the simulated temperature and current density distributions for die thicknesses of 7 mm, 14 mm, and 28 mm. The current density distribution pattern within the punch and the sample remains largely unchanged by variations in die wall thickness, although noticeable effects are observed within the die itself. The current density distribution reveals a high current concentration at the outer edges of the graphite punch. This phenomenon, commonly referred to as current crowding, is a direct geometric consequence of the tooling assembly. Here, the current lines converge as they pass from the wider spacer into the narrower punch, causing the current density to be highest at the region of the punch where the cross-sectional area is smallest. In all cases, the maximum current density coincides with the maximum temperature at the center of the punch, confirming that Joule heating is the dominant heat source in this region. In contrast, the current density within the graphite die is significantly lower than in the punch and the TiB_2 sample. This is primarily due to the introduction of an electrical contact resistance (ECR) by the graphite sheet. The sheet acts as a resistive barrier, effectively directing the electric current away from the die and forcing it to flow through the electrically conductive TiB_2 sample. This forced current focusing is a key mechanism for energy efficiency. The observation that the current density within the graphite sheet itself is higher than in the die confirms that the sheet is an active part of the circuit.

The presence of the graphite sheet also has a significant thermal impact. The graphite sheet is consistently hotter than the surrounding graphite die. This indicates that the sheet acts as a thermal barrier, trapping a portion of the Joule heat generated in the sample and preventing its efficient transfer to the die wall, where it would be lost to the environment via radiation. This heat-trapping effect is crucial for maintaining a high sample temperature and is beneficial for the overall energy efficiency of the SPS process. As expected for a conductive sample, the sheet's ability to both focus on the current and trap heat leads to a significant increase in process efficiency. The temperature distribution on the die surface reveals that the maximum temperature consistently occurs at the outer radial edge, precisely at the sample/die interface. This indicates that the interface between the TiB_2 sample, the graphite sheet, and the die is the principal source of heat flowing into the die. The improved contact conditions at this interface, which reduce thermal contact resistance (TCR), facilitate greater heat flow. Consequently, the die thickness has an inverse relationship with its surface temperature. The thinnest die (7 mm) exhibits the highest die surface temperature, while the temperature progressively drops as the

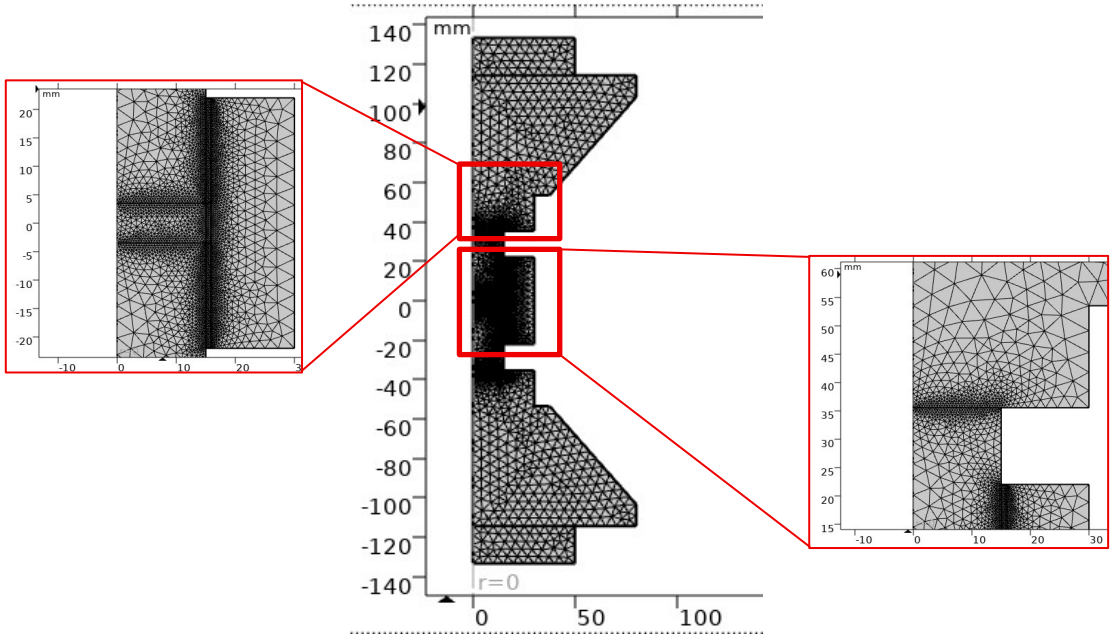

Fig. 3. Generated mesh of the SPS assembly showing element distribution and refinement zones.

die thickness increases to 28 mm. A thicker die wall provides a larger cross-sectional area for current flow, which reduces the current density and thus lowers the volumetric Joule heating within the die itself. However, the increased thermal mass and larger surface area of the thicker die lead to greater heat absorption and radiative losses, resulting in higher overall energy consumption. Conversely, the thinner die wall leads to higher current density and temperature but also exhibits lower radiative losses and better thermal uniformity, making it more energy-efficient overall. The primary source of the temperature gradient within the TiB_2 sample is confirmed to be the sample/sheet/die interface. The upper surface of the punch, which is in contact with the spacer, exhibits a lower temperature. Furthermore, the TCR at the punch/spacer interface effectively prevents heat from flowing back toward the spacer and cooling system and traps it inside the punches.

3.1.2. Effect of die height (h)

Unlike die thickness, the die height has a profound and decisive impact on both current density and temperature patterns, as illustrated in Fig. 5. This strong influence arises because the height directly determines the contact area between the punch and the die, which is the main pathway for current flow and heat transfer. When the die height is reduced to 11 mm, several important changes are observed. The current density in the punch and the sample increases markedly, a direct consequence of the reduced cross-sectional area available for current flow. The maximum temperature remains at the punch, but the hot region shifts closer to the sample. This is highly beneficial because it reduces the radial temperature gradient within the sample and improves heat conduction from the punch to the sample, leading to better thermal uniformity. The temperature of the graphite sheet rises considerably,

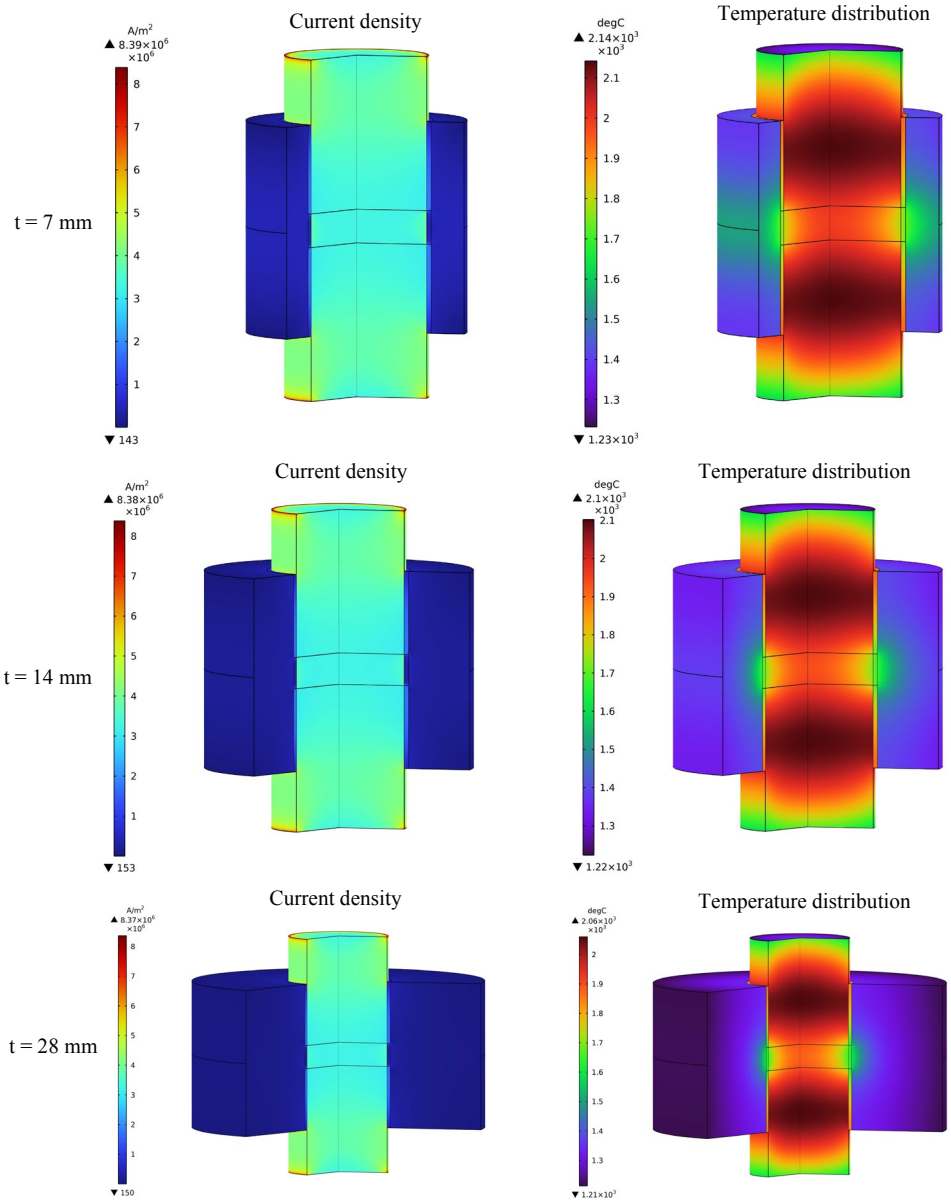

Fig. 4. Simulated temperature distributions and current density contours for die thicknesses of 7 mm, 14 mm, and 28 mm.

indicating that it effectively traps heat, via thermal contact resistance, inside the punch and sample. In addition, the die surface temperature also increases significantly. The higher die surface temperature in the shorter die is a direct consequence of its smaller thermal mass and the concentrated Joule heating in the punch and sample.

When the die height is increased to 35 mm, these trends reverse. The current density in the punch and the sample decreases substantially, the hot region remains inside the punch away from the sample, the radial temperature gradient across the sample becomes much larger, and the graphite sheet and die surface remain cooler, implying that less heat is retained in the sample.

The fundamental reason why die height dominates over die thickness is that height directly controls the contact area between the punch and the die, which is the primary conduit for both electricity and heat. Any variation in height alters the resistance at this critical interface, thereby strongly affecting current distribution, Joule heating, and ultimately the temperature field. In contrast, changing the die thickness only modifies the lateral cross-section of the die, which plays a minor role.

3.2. Quantitative evaluation of temperature changes at different thicknesses and heights

Fig. 6 presents a quantitative evaluation of the temperature as a

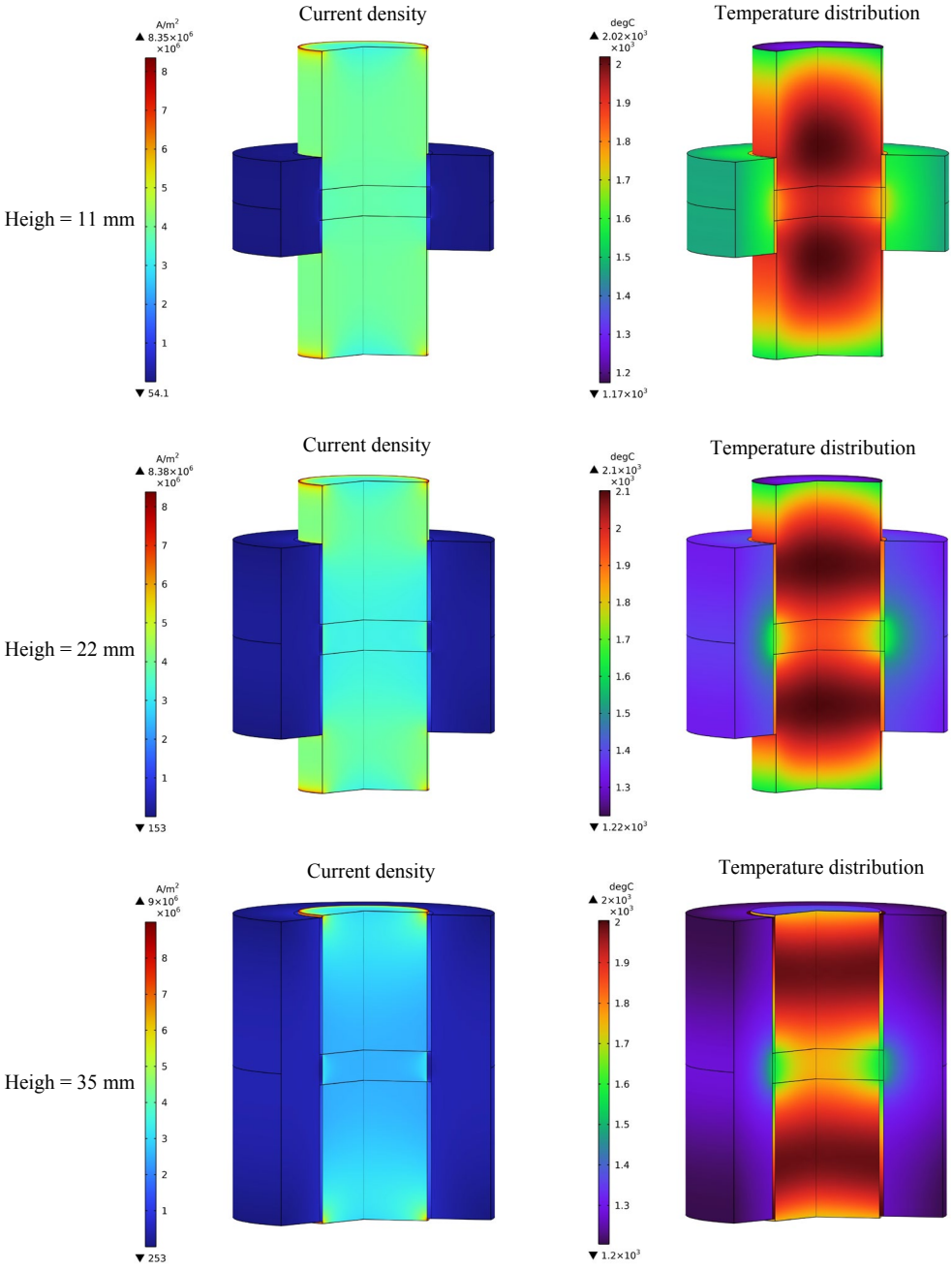

Fig. 5. Simulated temperature distributions and current density contours for die heights of 11 mm, 22 mm, and 35 mm.

function of die thickness and die height. As shown in Figs. 6a & 6b, the temperature consistently decreases from the sample center toward the die surface, but the radial gradient is significantly more sensitive to variations in die height than to thickness.

With increasing die thickness (Fig. 6c), the sample center temperature (point C) drops from 1992 °C to 1878 °C (a 114 °C reduction), while the die surface temperature (point B) declines more sharply from 1543 °C to 1220 °C (a 323 °C reduction). The maximum punch temperature decreases from 2142 °C to 2060 °C, and the radial temperature difference across the sample rises slightly from 204 °C to 221 °C. As shown in Fig. 6d, increasing die height from 11 mm to 22 mm leaves the sample center temperature nearly unchanged (1932 °C to 1936 °C), but further increasing it to 35 mm causes a substantial drop to 1754 °C. The die surface temperature decreases continuously from 1472 °C to 1280 °C. The maximum punch temperature rises from 2019 °C to 2102 °C as height increases to 22 mm, then falls to 1988°C at 35 mm. The radial temperature difference follows a non‑linear trend. It increases from 169 °C to 213 °C at 22 mm, then declines to 186 °C at 35 mm. This decline, however, does not indicate improved thermal uniformity; it merely reflects the significant cooling of the sample center, bringing it closer to the cooler die surface. Sensitivity analysis reveals that die thickness reduces all monitored temperatures in a nearly linear manner, with the die surface showing the highest sensitivity. Die height, in contrast, exhibits a non‑linear and more complex effect: moderate height (h = 22 mm) increases punch temperature and maintains sample center temperature but widens the radial gradient, while excessive height leads to substantial heat loss and a sharp drop in sample temperature. Overall, the height of the die has a stronger influence on sample center and punch temperatures, whereas die thickness primarily governs the die surface temperature.

3.3. Effect of die thickness and height on heating rate

The heating rate is a critical parameter in the SPS process because it directly influences densification kinetics, microstructural evolution, and final material properties. In this study, the heating rates at two key locations were examined: the sample center (point C) and the die surface (point B). Fig. 7 presents the heating rates obtained for three die thicknesses (7 mm, 14 mm, and 28 mm) and three die heights (11 mm, 22 mm, and 35 mm), all under the same electrical input conditions.

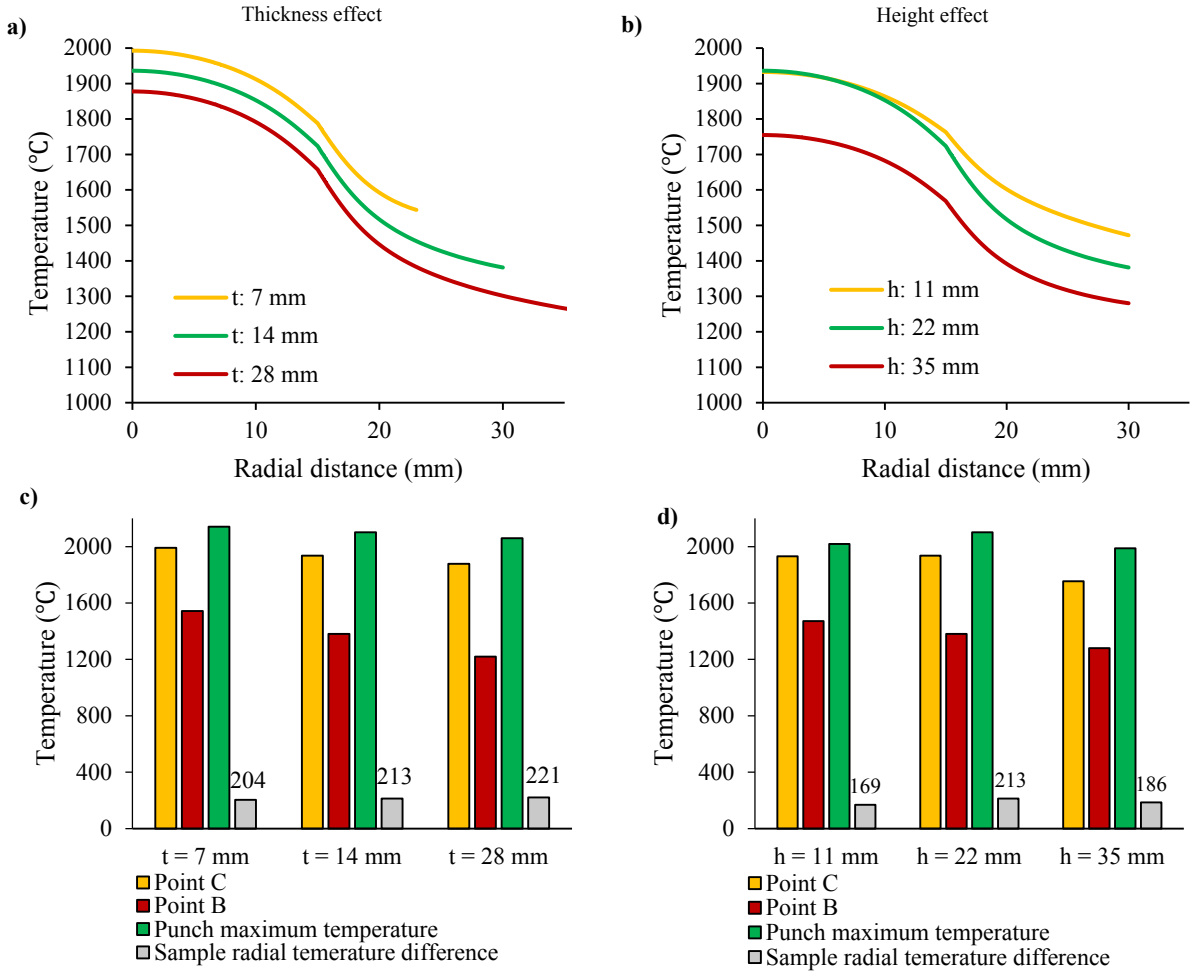

Fig. 6. a, c) Radial temperature distribution and temperatures at key points for different die thicknesses, and b, d) radial temperature distribution and temperatures at key points for different die heights.

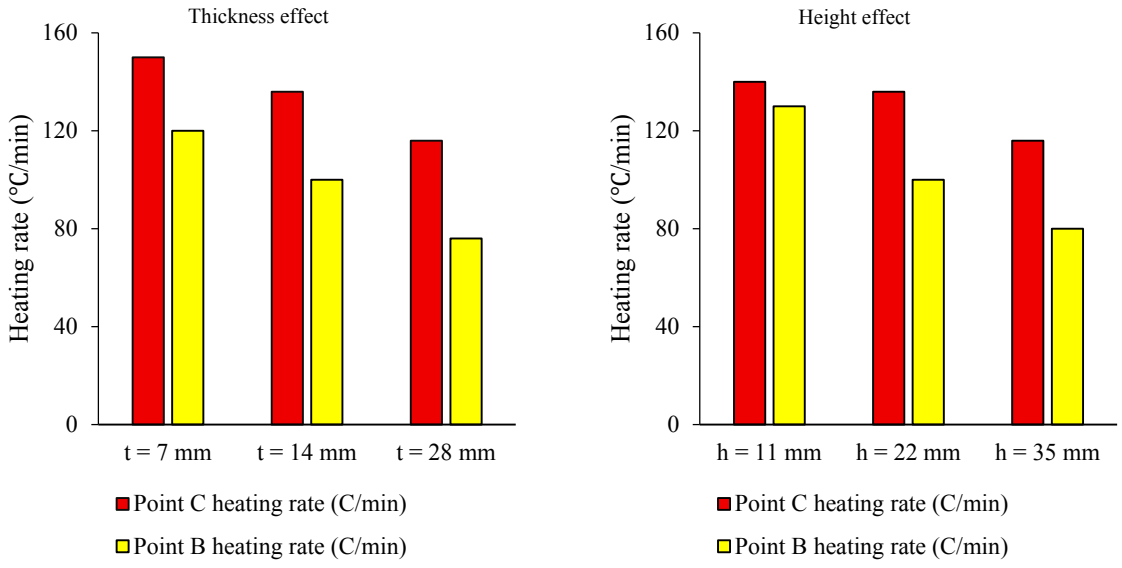

Fig. 7. Heating rates at the sample center (point C) and die surface (point B) for different die thicknesses and heights.

3.3.1. Effect of die thickness

As the die wall thickness increases from 7 mm to 28 mm, the heating rate at the sample center progressively decreases from 150 °C/min to 116 °C/min, a reduction of approximately 23%. Simultaneously, the heating rate at the die surface drops from 120 °C/min to 76 °C/min, a more pronounced decrease of about 37%. Two mechanisms explain these trends. First, a thicker die has a larger cross-sectional area for current flow. For a fixed total current, increasing the cross-section reduces the current density (J = I/A) in the die wall. Since the volumetric Joule heating power density is proportional to J^2, a lower current density leads to less heat generation per unit volume within the die itself. Second, a thicker die has a greater volume of graphite and a larger external surface area. More material must be heated to raise its temperature, and the larger surface area increases radiative heat loss to the surroundings. Both effects mean that a thicker die absorbs more of the total Joule heat produced, leaving less energy available to raise the temperature of the sample and the punch. The sample center therefore heats more slowly, and the die surface temperature rises even more slowly because the die not only loses heat but also has a larger thermal mass. The widening gap between the two heating rates indicates that the die surface suffers a larger relative reduction because its temperature rise depends on both its own internal heating and the heat conducted from the sample, both of which are diminished.

3.3.2. Effect of die height

The influence of die height is more complex and, in certain aspects, more significant. When the die height is reduced to 11 mm, the heating rate at the sample center is 140 °C/min, only slightly lower than the maximum observed (150 °C/min for the thinnest die). Remarkably, the heating rate at the die surface is 130 °C/min, yielding a very small difference of just 10 °C/min between the sample center and the die surface. As the die height increases to 22 mm, the sample center heating rate falls to 136 °C/min, and the die surface rate drops to 100 °C/min, widening the difference to 36 °C/min. At the largest height (35 mm), the sample center heating rate further decreases to 116 °C/min, and the die surface rate reaches 80 °C/min, maintaining a difference of 36 °C/min.

The critical factor here is the change in the cross-sectional area of the current path through the punch/die interface. The die height directly determines the contact area between the punch and the die wall. A shorter die reduces the vertical contact length, which decreases the total cross-section available for current to flow from the punch into the die. Consequently, the electrical contact resistance at this interface effectively becomes larger, forcing a larger fraction of the total current to remain in the punch and flow through the conductive sample rather than diverging into the die. This current focusing effect increases the current density in the punch and sample, which in turn raises the volumetric Joule heating rate in those components. As a result, the temperature of the sample and the punch increases at a higher rate. The heat generated in the punch and sample is then conducted to the die surface, and because the die itself carries less direct current, its own internal Joule heating is reduced. However, the intense heat flux from the sample/punch region to the die surface, combined with the shorter conductive path, causes the die surface to heat up almost as quickly as the sample center. This explains the exceptionally small difference of only 10 °C/min at h = 11 mm. As the die height increases, the longer contact area allows more current to flow into the die wall, reducing the current density in the punch and sample and increasing the direct Joule heating within the die. The sample therefore heats more slowly, and the die surface temperature rise becomes more dependent on its own internal heating. But because the die has a larger volume to heat (greater height), its heating rate drops sharply. Consequently, the heating rate difference widens.

When comparing the two geometric parameters, die thickness mainly affects the absolute heating rate through thermal mass and heat loss, with thinner walls giving faster heating because less graphite needs to be heated and less heat is extracted from the sample. Die height, on the other hand, strongly influences the distribution of current between the sample/punch and the die, thereby controlling both the heating rate of

the sample and the thermal uniformity between the sample and the die. The shortest die (11 mm) forces the current to focus in the sample, achieving a high sample heating rate (140 °C/min) and the best thermal homogeneity (only 10 °C/min difference). For applications where microstructural uniformity is the primary goal, reducing die height is therefore a more effective strategy than reducing die thickness. If maximum heating rate is the sole priority, the thinnest die (7 mm) offers the fastest sample heating (150 °C/min), but with a larger temperature difference (30 °C/min). An optimal design might combine a moderately thin die with a short height to balance heating rate and thermal homogeneity.

3.4. Effect of die thickness and height on die losses and power consumption

Radiative heat losses from the die surface are a key contributor to the overall energy balance in the SPS process, as it directly represents the thermal energy dissipated to the surroundings. Fig. 8 presents the calculated radiative heat losses from the outer surface of the graphite die for three different die thicknesses (t = 7 mm, 14 mm, and 28 mm) and three different die heights (h = 11 mm, 22 mm, and 35 mm), all under constant target temperature conditions (1900 °C at point C). As the die thickness increases, the heat loss rises gradually from 2351 W to 2792 W. This is attributed to the larger outer surface area and the improved thermal conduction path from the hot sample to the die surface, which maintains a higher die surface temperature.

The influence of die height is substantially stronger. Increasing the height from 11 mm to 35 mm raises the heat loss from 1675 W to 3592 W, more than doubling the loss. This sharp increase is due to the direct proportional relationship between the lateral surface area and the height. The sensitivity to height is higher than that of thickness. Notably, the lowest height (11 mm) exhibits the smallest heat loss (1675 W), indicating superior thermal efficiency. These results demonstrate that die height is the dominant geometric parameter controlling radiative losses, and reducing height is the most effective strategy for minimizing energy dissipation in the SPS process.

To maintain a constant sample center temperature of 1900 °C, the required electric current and resulting power consumption were calculated for three die thicknesses (7, 14, and 28 mm) and three die heights (11, 22, and 35 mm). As the die thickness increases from 7 mm to 28 mm, the required current rises from 2693 A to 2832 A (2765 A for t = 14 mm). This increase is relatively modest (about 5%), indicating that thicker walls demand slightly more current to compensate for the larger thermal mass and increased radiative losses. For the die height, increasing the height from 11 mm to 22 mm leaves the current unchanged at 2765 A. However, a further increase to 35 mm raises the current sharply to 2983 A, which is approximately 8% higher than at 11 mm. This sharp rise reflects the significant additional heat loss through the enlarged die surface, which must be compensated by higher electrical input.

The power consumption is presented in Fig. 9. As die thickness increases from 7 mm to 28 mm, the required power rises steadily from 9596 W to 10600 W. A thicker die increases the cross-sectional area available for current flow, which reduces the current density and thus lowers the volumetric Joule heating within the die itself, it also provides a larger surface area for radiative heat loss and a greater thermal mass to be heated. The net effect is an overall increase in power demand to maintain the target temperature.

Increasing the height from 11 mm to 22 mm reduces the power requirement from 10569 W to 10103 W, a decrease of about 4.4%. However, further increasing the height to 35 mm results in a negligible change. This trend can be explained by two competing mechanisms. First, a taller die encloses a larger portion of the punch, reducing its radiative heat flux to the cold chamber walls and trapping the heat within the punches. This trapping effect lowers the heat loss from the punch, which is the hottest component, and helps retain thermal energy within the system. Second, the graphite sheet placed between the punch and the die acts as a thermal barrier, limiting conductive heat transfer to the die. These combined effects improve the overall thermal efficiency of the system, allowing the same target temperature to be achieved with less electrical input. However, as the die height increases further, the lateral surface area of the die also increases, leading to higher radiative losses from the die itself. Beyond a certain height, this additional loss begins to outweigh the heat-trapping benefit. At 35 mm, the power consumption remains similar to the 22 mm case, indicating that the system has reached a point where further height increase does not yield additional energy savings.

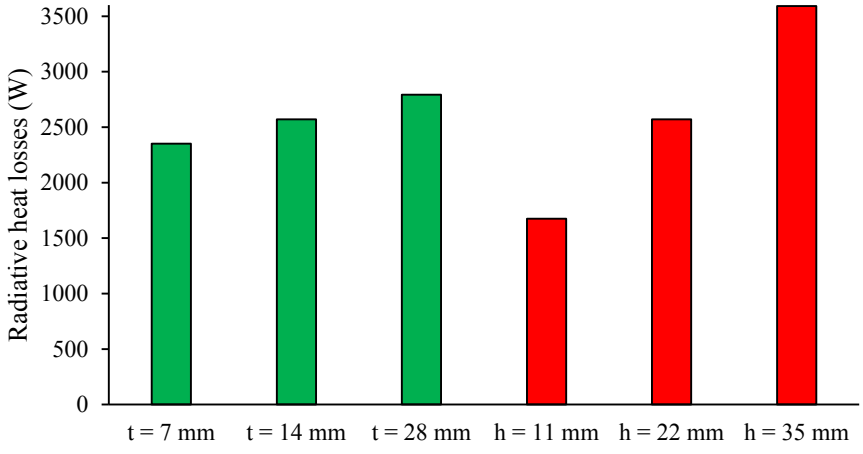

Fig. 8. Radiative heat losses from the die surface for different die thicknesses and die heights.

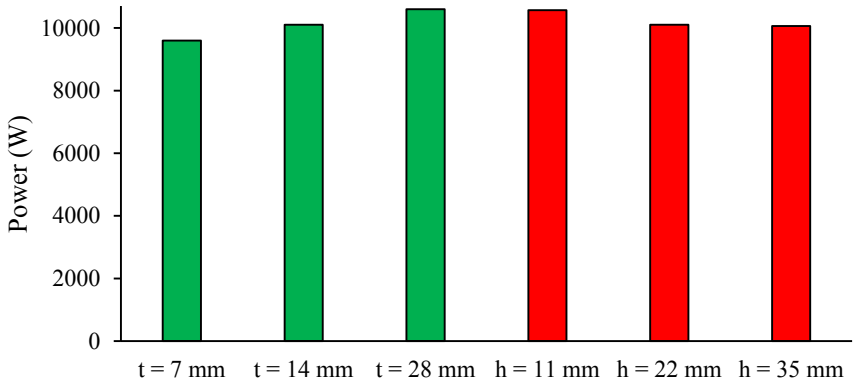

Fig. 9. Power consumption required to achieve a constant sample center temperature of 1900 °C for different die thicknesses and die heights.

The lowest power consumption is achieved with the thinnest die (7 mm), at 9596 W. This geometry also exhibits the lowest radiative loss from the die surface (2351 W) and the smallest radial temperature gradient (204 °C), indicating that the thinnest die offers the best combination of energy efficiency and thermal uniformity among the thicknesses examined. For die height, the optimal value appears to be around 22 mm, which provides the best compromise between heat trapping within the punches and limiting die surface radiation losses. Zhang et al. [11] reported a radial temperature gradient of up to 155 °C at thermal steady state for B_4C, attributing it to radiative heat loss from the die surface. They also found that reducing the mold diameter improved thermal efficiency without significantly affecting the gradient. The present study is consistent with their attribution of the radial gradient to radiation losses and further extends these findings by revealing that die height is the dominant geometric parameter, exerting a substantially stronger influence on both thermal gradients and energy consumption than thickness or diameter. Moghanlou et al. [26] investigated the effect of graphite die geometry on energy consumption during SPS of conductive ZrB_2. They reported that increasing die height raises power demand due to higher electrical resistance. Thicker dies require more energy but have a negligible effect on thermal homogeneity. They also confirmed that radiative loss from the die surface is the dominant heat dissipation mechanism. The present study on conductive TiB_2 is fully consistent with these findings. The observed trends, increased power consumption with larger die height and thickness, and the dominant role of radiative losses, are in complete agreement with their results. This consistency validates the reliability of the present numerical model and confirms that the underlying physical mechanisms governing energy consumption and thermal distribution are similar for conductive UHTC systems.

4. Conclusions

The optimization of spark plasma sintering for conductive TiB_2 ultra-high temperature ceramics requires resolving the complex interplay between electro‑thermal coupling, contact resistances, and geometric design. This study establishes a validated coupled electro‑thermal finite element model that incorporates both electrical and thermal contact resistances with graphite sheet interlayers, enabling the evaluation of die wall thickness and die height effects on current and thermal distribution and energy consumption. The findings demonstrate that die height exerts substantially stronger influence than wall thickness, fundamentally because height controls the contact area between punch and die, thereby governing current distribution between the conductive sample and the tooling. Increasing die height from 11 mm to 35 mm reduces sample center temperature from 1932 °C to 1754 °C and more than doubles radiative loss from the die lateral surface. The heating rate analysis reveals that the shortest die (11 mm height) achieves a sample center heating rate of 140 °C/min and a die surface heating rate of 130 °C/min, yielding a difference of only 10 °C/min, which represents the best thermal homogeneity. In contrast, increasing wall thickness from 7 mm to 28 mm reduces the sample center heating rate from 150 °C/min to 116 °C/min and lowers the die surface heating rate from 120 °C/min to 76 °C/min, while the difference between the two locations widens from 30 °C/min to 40 °C/min. This comparison indicates that die height predominantly governs current focusing and thermal uniformity through control of the punch‑die contact area, whereas thickness primarily modulates the absolute heating rates through thermal mass and radiative loss effects. The power consumption analysis identifies the thinnest die (7 mm) as the most energy‑efficient configuration, requiring 9596 W to maintain 1900 °C at the sample center, while a moderate height of 22 mm minimizes power demand through effective shielding of the punch and heat accumulation inside it, with further height increase to 35 mm yielding no additional energy saving due to offsetting die surface losses.

CRediT authorship contribution statement

Ramin Meshkabadi: Project administration, Conceptualization, Writing-review & editing.
Milad Sakkaki: Writing – original draft, Methodology, Software, Validation.
Vahid Pouyafar: Supervision, Conceptualization, Investigation.

Data availability

The data underlying this article will be shared on reasonable request to the corresponding author.

Declaration of competing interest

The authors declare no competing interests.

Funding and acknowledgment

This research was supported by the University of Mohaghegh Ardabili (Research grant number: 9351).

References

[1] W.G. Fahrenholtz, E.J. Wuchina, W.E. Lee, Y. Zhou, Ultra-High Temperature Ceramics, Materials for Extreme Environment Applications, The American Ceramic Society, Wiley. (2014). https://doi.org/10.1002/9781118700853.

[2] B.C. Wyatt, S.K. Nemani, G.E. Hilmas, E.J. Opila, B. Anasori, Ultra-high temperature ceramics for extreme environments, Nat. Rev. Mater. 9 (2023) 773–789. https://doi.org/10.1038/s41578-023-00619-0.

[3] D. Sciti, L. Silvestroni, V. Medri, F. Monteverde, Sintering and Densification Mechanisms of Ultra-High Temperature Ceramics, Ultra-High Temperature Ceramics, Wiley. (2014) 112−143. https://doi.org/10.1002/9781118700853.ch6.

[4] A. Ruys, O. Gingu, G. Sima, S. Maleksaeedi, Powder Processing of Bulk Components in Manufacturing, Handbook of Manufacturing Engineering and Technology, London: Springer, London. (2013) 1–69. https://doi.org/10.1007/978-1-4471-4976-7_48-4.

[5] T.N. Maity, N.K. Gopinath, K. Biswas, B. Basu, Spark Plasma Sintering of Ultrahigh Temperature Ceramics, Spark Plasma Sintering of Materials, Springer International Publishing. (2019). https://doi.org/10.1007/978-3-030-05327-7_13.

[6] A.M. Laptev, M. Bram, D. Garbiec, J. Räthel, A. van der Laan, et al., Tooling in Spark Plasma Sintering Technology: Design, Optimization, and Application, Adv. Eng. Mater. 26 (2024) 2301391. https://doi.org/10.1002/adem.202301391.

[7] P. Cavaliere, B. Sadeghi, A. Shabani, Spark Plasma Sintering: Process Fundamentals, Spark Plasma Sintering of Materials, Cham: Springer International Publishing. (2019) 3–20. https://doi.org/10.1007/978-3-030-05327-7_1.

[8] A. Bellosi, F. Monteverde, D. Sciti, Fast Densification of Ultra-High-Temperature Ceramics by Spark Plasma Sintering, Int. J. Appl. Ceram. Technol. 3 (2006) 32–40. https://doi.org/10.1111/j.1744-7402.2006.02060.x.

[9] J.P. Kelly O.A. Graeve, Spark Plasma Sintering as an Approach to Manufacture Bulk Materials: Feasibility and Cost Savings, JOM. 67 (2015) 29–33. https://doi.org/10.1007/s11837-014-1202-x.

[10] M. Sakkaki, F. Sadegh Moghanlou, M. Vajdi, M. Shahedi Asl, M. Mohammadi, M. Shokouhimehr, Numerical simulation of heat transfer during spark plasma sintering of zirconium diboride, Ceram. Int. 46 (2020) 4998–5007. https://doi.org/10.1016/j.ceramint.2019.10.240.

[11] S. Zhang, W. Liu, W. Wang, Y. Gao, A. Wang, et al., Numerical Simulation of Physical Fields during Spark Plasma Sintering of Boron Carbide, Materials (Basel). 16 (2023) 3967. https://doi.org/10.3390/ma16113967.

[12] G. Lee, E.A. Olevsky, C. Manière, A. Maximenko, O. Izhvanov, et al., Effect of electric current on densification behavior of conductive ceramic powders consolidated by spark plasma sintering, Acta Mater. 144 (2018) 524–533. https://doi.org/10.1016/j.actamat.2017.11.010.

[13] C. Manière, L. Durand, E. Brisson, H. Desplats, P. Carré, et al., Contact resistances in spark plasma sintering: From in-situ and ex-situ determinations to an extended model for the scale up of the process, J. Eur. Ceram. Soc. 37 (2017) 1593–1605. https://doi.org/10.1016/j.jeurceramsoc.2016.12.010.

[14] C. Manière, A. Pavia, L. Durand, G. Chevallier, K. Afanga, C. Estournès, Finite-element modeling of the electro-thermal contacts in the spark plasma sintering process, J. Eur. Ceram. Soc. 36 (2016) 741–748. https://doi.org/10.1016/j.jeurceramsoc.2015.10.033.

[15] M. Fattahi, M. Najafi Ershadi, M. Vajdi, F. Sadegh Moghanlou, A. Sabahi Namini, M. Shahedi Asl, On the simulation of spark plasma sintered TiB2 ultra high temperature ceramics: A numerical approach, Ceram. Int. 46 (2020) 14787–14795. https://doi.org/10.1016/j.ceramint.2020.03.003.

[16] B. Basu, G.B. Raju, A.K. Suri, Processing and properties of monolithic TiB 2 based materials, Int. Mater. Rev. 51 (2006) 352–374. https://doi.org/10.1179/174328006X102529.

[17] X. Lv, Z. Yin, Z. Yang, J. Chen, S. Zhang, et al., Review on the Development of Titanium Diboride Ceramics, Recent Prog. Mater. 06 (2024) 1–48. https://doi.org/10.21926/rpm.2402009.

[18] M. Shojaie-bahaabad, M. Bozorg, M. Najafizadeh, P. Cavaliere, Ultra high temperature ceramic coatings in thermal protection systems (TPS), Ceram. Int. 50 (2024) 9937–9951. https://doi.org/10.1016/j.ceramint.2023.12.372.

[19] J.R. Ramberg, C.F. Wolfe, W.S. Williams, Resistance of Titanium Diboride to High-Temperature Plastic Yielding, J. Am. Ceram. Soc. 68 (1985) C-78–C-79. https://doi.org/10.1111/j.1151-2916.1985.tb09637.x.

[20] L. Tang, B. Lin, B. Zhang, D. Zhang, Y. Gong, N. Xiong, Research Status of Titanium Diboride High Temperature Ceramics, J. Phys.: Conf. Ser. 2200 (2022) 012024. https://doi.org/10.1088/1742-6596/2200/1/012024.

[21] X. Wang, S.R. Casolco, G. Xu, J.E. Garay, Finite element modeling of electric current-activated sintering: The effect of coupled electrical potential, temperature and stress, Acta Mater. 55 (2007) 3611–3622. https://doi.org/10.1016/j.actamat.2007.02.022.

[22] Y. Achenani, M. Saâdaoui, A. Cheddadi, G. Bonnefont, G. Fantozzi, Finite element modeling of spark plasma sintering: Application to the reduction of temperature inhomogeneities, case of alumina, Mater. Des. 116 (2017) 504–514. https://doi.org/10.1016/j.matdes.2016.12.054.

[23] X. Wei, D. Giuntini, A.L. Maximenko, C.D. Haines, E.A. Olevsky, Experimental Investigation of Electric Contact Resistance in Spark Plasma Sintering Tooling Setup, J. Am. Ceram. Soc. 98 (2015) 3553–3560. https://doi.org/10.1111/jace.13621.

[24] C. Maniere, A. Pavia, L. Durand, G. Chevallier, V. Bley, et al., Pulse analysis and electric contact measurements in spark plasma sintering, Electr. Power Syst. Res. 127 (2015) 307–313. https://doi.org/10.1016/j.epsr.2015.06.009.

[25] R.M. German, Powder Metallurgy and Particulate Materials Processing: The Processes, Materials, Products, Properties and Applications, Metal Powder Industries Federation, United States. (2005).

[26] F. Sadegh Moghanlou, M. Vajdi, M. Sakkaki, S. Azizi, Effect of graphite die geometry on energy consumption during spark plasma sintering of zirconium diboride, Synth. Sinter. 1 (2021) 54–61. https://doi.org/10.53063/synsint.2021.117.